

Alma Mater Studiorum Università di Bologna  
Archivio istituzionale della ricerca

Numerical simulation of the compression crushing energy of carbon fiber-epoxy woven composite structures

This is the final peer-reviewed author's accepted manuscript (postprint) of the following publication:

*Published Version:*

Rondina F., Falaschetti M.P., Zavatta N., Donati L. (2023). Numerical simulation of the compression crushing energy of carbon fiber-epoxy woven composite structures. COMPOSITE STRUCTURES, 303, 1-15 [10.1016/j.compstruct.2022.116300].

*Availability:*

This version is available at: <https://hdl.handle.net/11585/899384> since: 2024-05-08

*Published:*

DOI: <http://doi.org/10.1016/j.compstruct.2022.116300>

*Terms of use:*

Some rights reserved. The terms and conditions for the reuse of this version of the manuscript are specified in the publishing policy. For all terms of use and more information see the publisher's website.

This item was downloaded from IRIS Università di Bologna (<https://cris.unibo.it/>).  
When citing, please refer to the published version.

(Article begins on next page)

# Numerical simulation of the compression crushing energy of carbon fiber-epoxy woven composite structures.

Francesco Rondina<sup>a,\*</sup>, Maria Pia Falaschetti<sup>a,b</sup>, Nicola Zavatta<sup>b</sup>, Lorenzo Donati<sup>a,b</sup>

<sup>a</sup> Department of Industrial Engineering, University of Bologna, Viale Risorgimento 2, 40136 Bologna, Italy.

<sup>b</sup> Interdepartmental Center for Industrial Research on Advanced Applications in Mechanical Engineering and Materials Technology, CIRI-MAM, University of Bologna, Viale Risorgimento 2, 40136 Bologna, Italy.

\* Corresponding author

## Abstract

The crashworthiness of composites is investigated in an experimental campaign and simulated using the explicit Finite Element solver ESI-VPS. Two damage models, derived from Ladevèze and Waas-Pineda, are implemented in modified forms, to work with woven-fabrics. The former uses conventional continuum damage formulations, while the latter introduces a traction-separation law to simulate cracks with prescribed fracture energies. The Waas-Pineda approach aims to simplify the material card definition and make the calibration more straightforward. Characterization tests are carried out on specimens manufactured with plain weave carbon fiber-epoxy tape. Notched coupons are analysed, as these tests are representative of the conditions observed during crushing of a composite structure. Innovative procedures to calibrate the damage models are introduced to remove, where possible, the need for iterative tuning. Once implemented, the calibrated material cards are validated against quasi-static crushing of corrugated specimens with two different layups. In the Waas-Pineda model, mesh objectivity is obtained only after correction of the modal fracture energies, instead, the Ladevèze model formulation is already consistent at different scale lengths. In addition, a sensitivity analysis shows a modest influence of friction coefficient and interlaminar fracture toughness. Results demonstrate that it is possible to obtain adequate results from both damage models when the proposed calibration strategy is used, but validation on test results is still advised to ensure the mesh discretization is suitable for the selected problems.

## Keywords

ESI-VPS, Crashworthiness, Damage Model Calibration, Carbon fabric, Fracture toughness

## 1. Introduction

Composite materials have been extensively used in many different industrial fields due to their competitive mechanical and physical characteristics. Thanks to their favorable strength-to-weight ratio and specific energy absorption (SEA), they represent an ally in the design of lightweight structures. Given the attention directed towards energy consumption and polluting emissions, efforts aimed at fuel-saving and increased payload are observed with great interest both in the automotive and aerospace industry.

Moreover, the advantageous properties of composite materials represent a step forward in the design of crashworthiness components. These materials have been shown to generate stable crushing at elevated SEA values, which can additionally be fine-tuned by modifying the layup, thickness and geometry, offering increased flexibility compared to metals. However, this flexibility often comes at the cost of complexity.

Many studies have been carried out in order to evaluate the influence of the resin and fiber materials [1–6], laminate stacking sequence and ply weaving [5,7,8], trigger [8–11], and cross-section geometries [4,5,7,8,11,12].

The matrix properties are relevant for crashworthy components design. Both thermoplastic and thermoset polymer matrices have been evaluated: Ramakrishna et al. [1] and Chang and Lees [2] demonstrated that thermoplastic matrices exhibited a higher specific energy absorption strictly connected with their higher Mode I toughness. However, Cauchi Savona and Hobbs [3] demonstrated that, for flat specimens, if Mode I fracture toughness is too high, a very steep and unwanted stress peak is observed. At the same time, for thermoset glass fiber [4] and carbon fiber [5] composites, it has been demonstrated that a higher SEA could be assured by using a high modulus and high strength matrix, rather than a tough one. On the other hand, the influence of the matrix on the SEA also depends widely on the kind of reinforcement: as reported by Jacob and al. [6], an increment in matrix failure strain results in an increase in absorption capability for brittle fiber reinforcements (e.g. carbon) while a decrease is observed for ductile fiber reinforcements (e.g. Kevlar). Therefore, the correct combination of fiber and matrix is important when the goal is to maximize energy absorption.

It is well known that in composite materials the load is mostly carried by the reinforcement. It would be logical, therefore, to use only unidirectional (UD) plies and monodirectional stacking sequences to maximize the energy absorption. However, it has been demonstrated that UD composites have an unstable failure mode, due to the lack of constraints that could reduce delamination growth [7]. Delamination failure, in fact, results in an energy absorption quite lower than that of a fragmentation mode. To investigate this effect on the SEA, Feraboli [5] studied different stacking sequences, founding out that a  $[0/\pm 45]_{ns}$  composite has a better SEA than a pure  $[\pm 45]_{ns}$  or  $[0/90]_{ns}$  configuration with the same thickness. Other studies have investigated the use of fabric prepreg instead of UD laminae. Due to fibers weaving, the fiber sliding phenomenon and splaying of outer plies can be neglected and the predominant failure mode becomes the fragmentation of fibers [8].

Fiber-reinforced materials usually have an elastic behavior which is beneficial to the rigidity and the dimension stability of components but leads to a fragile abrupt failure with resulting low energy absorption capability. However, composite components with a proper trigger result in a progressive failure mode which could absorb more energy than a common metal folding failure. Even metal crashworthy structures necessitate an initial defect to obtain a more efficient dissipation. Usually, a crimp can be found in metal crash components. For composite ones, a bevel or a saw tooth shape edge is typically used. Jiang et alii [9] studied many different kinds of triggers using numerical simulation. They found out that the  $45^\circ$  chamfer trigger maintains the highest sustained crush load and SEA while the wedge trigger (in the slanting and straight conformation) is effective in decreasing the initial peak load. A weakened lay-up is used as triggering system by Troiani et alii [8], Kohlgruber [10], and Hanagud et alii [11]. This consists of a ply drop-off trigger, a sector where one or more plies are cut out, located near the loading edge. This kind of trigger behaves differently from the chamfer: it is believed that the differences are related to the micro-mechanical effects on the failure mode at the micro-mechanical level.

The contribution of geometry to the crashworthiness of a structure depends on different parameters. Excessive unsupported height of a crashing flat structure, for example, could lead to a premature buckling failure and, consequently, to a low energy dissipation [12]. To remove this inconvenience, self-supporting structures are usually used in crashworthy components (like round tubes [7], square tubes [4], and truncated cones [13]). A corrugated geometry, close to the engineering application but easier to produce than tubes or cones, has been found extensively in the literature [5,8,11]. Hanagud et al. [11] presented a study of the sensibility of the curvature of a corrugated specimen on the specific energy absorption. Many different

cross-sections are investigated, starting from the flat coupon, passing through different sinusoidal shapes, to a semicircular corrugated geometry. It is concluded that a semicircular section has a higher specific sustained crush stress than the other configurations, especially compared to the flat or the low-angle sinusoidal geometries, which occur in a buckling phenomenon if not correctly sustained.

Experimental tests on full-scale components are quite expensive. To overcome this inconvenience, several predictive damage models have been developed, mostly based on a Finite Element Method (FEM) formulation. These models usually require several physical properties as an input, that need to be measured by experimental tests. Moreover, these numerical models must be calibrated and, therefore, are valid only for specific conditions. Different damage models could be used for different applications. The main damage models can be divided into three groups: Progressive Failure Model (PFM), Continuum Damage Models (CDM), and Non-local Damage Model (NDM).

Progressive Failure Models are usually found in large-scale simulations. Implementations of these models use failure criteria like Chang and Chang [14] and Tsai-Wu [15] to drive an algorithm for element elimination. Due to their nature, these models do not capture the complexity of the crushing phenomena: their accuracy depends on extensive calibration and requires the adjustment of numerical parameters to control the crush energy.

In Continuum Damage Models the material softening is implemented through internal variables to deteriorate the mechanical properties. This is done by introducing damage variables into the constitutive equations, to decrease material stiffness through damage evolution functions. In this case, there is a higher level of detail than with PFMs.

The Non-local Damage Model is similar to CDM, but it can scale up to large simulations like PFM without any additional calibration. In these models, the effect of cracks is smeared across the finite element and treated using traction-separation formulations, effectively overcoming stress localization at discontinuities. NDM gained recent attention thanks to the convincing comparison with experimental crash applications.

In a previous work by Rondina and Donati [16], the crushing response of unidirectional carbon/epoxy corrugated coupons is simulated by means of ESI-VPS explicit solver. Two damage models, a CDM (Ladevèze [17–19]) and an NDM (Waas-Pineda [20]) are compared. It is demonstrated that the CDM formulation does have a limitation to maintain a stable simulation when large deformations occur. On the other hand, the non-local model can overcome this limitation. Moreover, with the Ladevèze model, there is a loss of contact between the specimen and the crashing plate due to element elimination; with Waas-Pineda this does not occur, and contact is assured throughout the simulation reducing load oscillations.

In this work, the crashworthiness properties of woven corrugated specimens are experimentally and numerically investigated. Specimens are made with a carbon/epoxy prepreg (GG285P Plain Weave fabric), and two stacking sequences are used ( $[0_f]_6$  and  $[45_f/45_f/0_f]_s$ ). Numerical models are implemented to predict the absorbed energy of the coupons, after calibration against relevant experimental tests. Two damage models are compared: a continuum damage mechanics model for an orthotropic fabric composite ([21], based on Ladevèze damage model for unidirectional composites [19]) and a non-local model (Waas-Pineda, modified for fabrics [20,22]).

## 2. Numerical Models

All finite element simulations are carried out in ESI-VPS commercial software. The laminate is modeled as a shell with plane stress formulation. The fabric-reinforced composite is defined as an orthotropic elastic-

plastic material, whose stiffness is gradually degraded by microcracking before failure. For this material, the in-plane stress and strain components are expressed as:

$$\begin{bmatrix} \varepsilon_{11} \\ \varepsilon_{22} \\ \varepsilon_{12} \end{bmatrix} = \begin{bmatrix} \frac{1}{E_{11}^0(1-d_{11})} & -\frac{\nu_{12}}{E_{11}^0} & 0 \\ -\frac{\nu_{12}}{E_{11}^0} & \frac{1}{E_{22}^0(1-d_{22})} & 0 \\ 0 & 0 & \frac{1}{G_{12}^0(1-d_{12})} \end{bmatrix} \begin{bmatrix} \sigma_{11} \\ \sigma_{22} \\ \sigma_{12} \end{bmatrix} \quad (1)$$

where  $E_{11}^0$ ,  $E_{22}^0$  and  $G_{12}^0$  are the elastic moduli of the undamaged material,  $d_{11}$ ,  $d_{22}$  are the damage parameters in the fiber directions and  $d_{12}$  is the damage parameter in the shear direction. These damage parameters vary from 0 for the pristine material to a value of 1 at ultimate failure. To account for the different material response to tension and compression loads, different elastic moduli  $E_{11c}^0$  and  $E_{22c}^0$  are considered for compression.

In the next sections, the two damage formulations implemented in the numerical model are presented.

### 2.1. Modified Ladevèze continuum damage model

A continuum damage model for unidirectional laminates was originally introduced by Ladevèze [17]. This model was then modified by Johnson et al. [21] to make it suitable for fabric-reinforced laminates. The model (LV) possesses the following features:

1. Fiber and matrix damage modes are assumed to be decoupled, with the former being driven by tension and compression loads and the latter by shear loads.
2. Fiber damage modes in tension and compression are different.
3. Distinct damage parameters are used in the two fiber directions.
4. The material is non-healing, i.e., accumulated damage is not recovered upon unloading and can only increase.

Condition 4 implies that the damage evolution reflects the maximum stress levels reached throughout the loading history; this condition can be imposed concisely as:  $d_{ij}(t) = \max_{\tau \leq t} \{d_{ij}(\tau)\}$ , where  $d_{ij}$  are the damage parameters defined below.

Following the framework identified by Ladevèze, the conjugate quantities governing the damage progression are defined as partial differences of the damaged strain energy  $E_D$  with respect to the damage parameters and are therefore analogous to energy release rates. For a woven fabric ply Johnson et al. [21] use three distinct damage scalars  $d_{11}$ ,  $d_{22}$  and  $d_{12}$ , relative to the two fiber directions and in-plane shear loading, with associated conjugate quantities  $Y_{11}^2$ ,  $Y_{22}^2$  and  $Y_{12}^2$  as defined in Eq. (2):

$$Y_{ij}^2 := \frac{\partial E_D}{\partial d_{ij}} = \frac{\sigma_{ij}^2(\tau)}{2E_{ij}^0(1-d_{ij}(\tau))^2}, \quad i, j \in \{1, 2\} \quad (2)$$

With the damage driving parameters defined as such, Johnson et alii found that the fiber-aligned damage accumulation functions,  $d_{11}$  and  $d_{22}$  evolve linearly with respect to the square root of the conjugate quantities:  $Y_{11}$  and  $Y_{22}$ , whereas the shear damage is found to fit linearly against the natural logarithm of

$Y_{12}$ . The VPS implementation reflects these findings and the functions in Eq. (3) are used for the damage accumulation of the lamina.

$$\begin{aligned}
 d_{11} &= \begin{cases} 0, & Y_{11} < Y_{110} \\ \frac{Y_{11} - Y_{110}}{Y_{11c}}, & Y_{110} < Y_{11} < Y_{11f} \end{cases} \\
 d_{22} &= \begin{cases} 0, & Y_{22} < Y_{110} \\ \frac{Y_{22} - Y_{110}}{Y_{11c}}, & Y_{110} < Y_{22} < Y_{11f} \end{cases} \\
 d_{12} &= \begin{cases} 0, & Y_{12} < Y_{120} \\ \frac{\ln(Y_{12}) - \ln(Y_{120})}{Y_{12c}}, & Y_{120} < Y_{12} < Y_{12f} \end{cases}
 \end{aligned} \tag{3}$$

Notably, the fiber-aligned damage modes share the same set of inputs for warp and weft directions but are distinct for tension and compression (identified hereafter by superscript  $c$ ). The complete set of damage inputs consists of twelve parameters, namely the stresses required for damage initiation,  $Y_{110}$ ,  $Y_{110}^c$  and  $Y_{120}$ , those at failure,  $Y_{11f}$ ,  $Y_{11f}^c$  and  $Y_{12f}$ , and interpolation coefficients  $Y_{11c}$ ,  $Y_{11c}^c$  and  $Y_{12c}$ . Post-damage ensues once the failure stress level is reached and acts as a limitation to the maximum transmissible stress. This requires the remaining three parameters:  $D_{11max}$ ,  $D_{11max}^c$  and  $D_{12max}$ . The determination of these parameters is accomplished by experimental tests.

The material response in the fiber directions is purely elastic so that the material returns to its initial state during unloading. On the other hand, the shear response, dominated by the matrix behavior, can exhibit a plastic behavior with permanent deformation. To introduce this effect, the total shear strain is split into elastic and plastic contributions:  $\varepsilon_{12} = \varepsilon_{el} + \varepsilon_p$ . To account for the matrix plastic strain, an elastic domain function  $F$  is introduced, which depends on the effective shear stress  $\sigma_{12}/(1 - d_{12})$  and an isotropic hardening term  $R(\varepsilon_p)$ , as described by Eq. (4). If the shear stress is below the yield criterion  $F < 0$ , the material remains under elastic deformation; beyond that, the plastic flow condition  $F = 0$  is satisfied by accumulation of plastic strain through the hardening function. In particular,  $R_0$  is the initial yield stress, and the hardening function follows the form identified by Johnson et alii [21] to fit well with test data for woven fabrics. The parameters  $m$  and  $\beta$  as well as the initial yield condition are determined from cyclic tensile loading tests on a  $[45_f]_n$  laminate; a detailed example of calibration for unidirectional ply model can be found in previous work from the authors [16].

$$\begin{aligned}
 F &= \frac{|\sigma_{12}|}{1 - d_{12}} - R(\varepsilon_p) - R_0 \\
 R(\varepsilon_p) &= \beta \varepsilon_p^m
 \end{aligned} \tag{4}$$

To improve the numerical stability, the elements must be eliminated if their damaged stiffness becomes too low. To solve this, an elimination criterion is introduced to remove the elements from the computation once a prescribed condition is reached. In the LV model, this condition is defined as a set of limit strains  $\varepsilon_{ij}^{lim}$  consisting of distinct values for positive and negative domains of each of the six  $ij$  components.

## 2.2. Waas-Pineda nonlocal damage model

Waas-Pineda model (WP) was originally described in [20,22]. This model combines the orthotropic elastic-plastic behavior of the LV with a nonlocal approach to include cracks in the continuum. The model can be used to describe the effects of both fiber and matrix failure, including phenomena such as fiber rupture and kinking, fiber-matrix debonding, and matrix cracking.

The model consists of three distinct material states: continuum state, cohesive state, and post-damage state. The transition from the continuum state to the cohesive (damaged) state is triggered by the failure criterion shown in Eq. (5), where five threshold values  $X_t$ ,  $X_c$ ,  $Y_t$ ,  $Y_c$  and  $Z_{12}$  are required.

$$\begin{aligned}
 \left(\frac{\sigma_{11}}{X_t}\right)^2 &\geq 1 & \sigma_{11} &\geq 0 \\
 \left(\frac{\sigma_{11}}{X_c}\right)^2 &\geq 1 & \sigma_{11} &< 0 \\
 \left(\frac{\sigma_{22}}{Y_t}\right)^2 &\geq 1 & \sigma_{22} &\geq 0 \\
 \left(\frac{\sigma_{22}}{Y_c}\right)^2 &\geq 1 & \sigma_{22} &< 0 \\
 \left(\frac{\sigma_{12}}{Z_{12}}\right)^2 &\geq 1 & &
 \end{aligned} \tag{5}$$

In the cohesive state, the material response is defined by a traction-separation law. The element stresses are computed as a function of the separation lengths  $\delta_{ij}$ , according to Eq. (6):

$$\sigma_{ij} = (1 - d_{ij})K_{ij}\delta_{ij} \tag{6}$$

where  $d_{ij}$  are the damage parameters and  $K_{ij}$  the cohesive stiffnesses. The separation lengths are calculated from the element dimensions  $l_{f1}$ ,  $l_{f2}$  along the main directions of orthotropy:

$$\begin{aligned}
 \delta_{11} &= l_{f1}\varepsilon_{11} \\
 \delta_{22} &= l_{f2}\varepsilon_{22} \\
 \delta_{12} &= (l_{f1} + l_{f2})(\varepsilon_{12} - \varepsilon_p)
 \end{aligned} \tag{7}$$

The element dimensions  $l_{f1}$  and  $l_{f2}$ , shown in Figure 1, are defined as the lengths of the lines parallel to the local fiber directions passing through the center of mass of the element and intersecting the two opposite edges of the element. Differently from the model proposed by Pineda [22], the implementation found in VPS does not calculate distinct damage conditions for each integration point within the element, but the damage is unique across its volume.

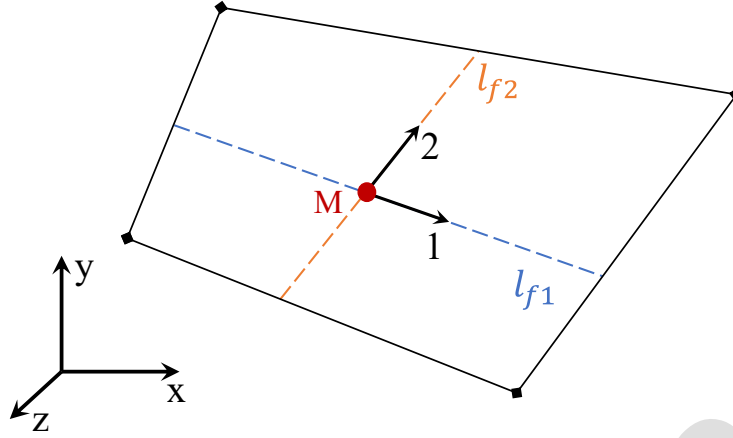


Figure 1: Representation of the internal element dimensions calculated for WP damage model: 1 and 2 are the fiber directions, and M is the center of mass of the element.

Damage evolution is defined by the following formula:

$$d_{ij} = \frac{\delta_{ij}^f (\delta_{ij}^{max} - \delta_{ij}^0)}{\delta_{ij}^{max} (\delta_{ij}^f - \delta_{ij}^0)} \quad (8)$$

where  $\delta_{ij}^{max} = \max_{\tau \leq t} \{|\delta_{ij}|\}$  is the maximum separation reached during previous loading history,  $\delta_{ij}^0$  is the initial separation at the transition to the cohesive state and  $\delta_{ij}^f$  is the separation at failure. For fiber damage modes  $d_{11}$ ,  $d_{22}$ , the separation at failure can be computed as  $\delta_{ii}^f = 2 G_{ICi} / \sigma_{ii}^0$ , being  $G_{ICi}$  the mode I fracture energy in the fibers directions and  $\sigma_{ii}^0$  the stress at the transition to the cohesive state. The different damage modes caused by tension and compression are accounted for by implementing two different fracture energies  $G_{ICi}$  and  $G_{ICi}^c$ , respectively. For matrix damage  $d_{12}$  it results that  $\delta_{12}^f = 2 G_{IIC} / \sigma_{12}^0$ , where  $G_{IIC}$  is the mode II fracture energy of the matrix and  $\sigma_{12}^0$  is the shear stress at transition.

Once the stresses  $\sigma_{ij}$  reach a lower threshold value, defined by  $1 - |\sigma_{ij} / \sigma_{ij}^0| \geq D_{max}$ , the elements enter a post-damage state, akin to the Ladevèze model. Finally, the elements are eliminated and removed from computation once a prescribed limit strain is reached. In this case,  $\epsilon_{lim}$  is defined as the square root of the second invariant of the deviatoric strain tensor.

In order for the numerical model to maintain the calibration parameters down to a reasonable number, the interaction between damage modes has not been taken into account; instead, the different damage modes activate and evolve independently following the criteria illustrated earlier. This additionally reduces the need for specialized testing at mixed-mode loading conditions, with a modest impact on performance and fidelity.

### 3. Materials and methods for model calibration

The input parameters of the numerical model are determined by experimental tests on composite specimens. To fully characterize the elastic-plastic and damage properties required by the model, several tests are conducted. The different test types and the input data they provide are summarized in Table 1.



**Table 1.** Types of tests conducted and corresponding direct input parameters of the LV and WP models.

Test type	Elastic-plastic properties	LV model	WP model
Cyclic tension 0°	$E_{11}^0, \nu_{12}$	$Y_{110}, Y_{11c}, Y_{11f}$	$X_t$
Static tension 90°	$E_{22}^0$		$Y_t$
Cyclic compression 0°	$E_{11c}^0$	$Y_{110}^c, Y_{11c}^c, Y_{11f}^c$	$X_c$
Static compression 90°	$E_{22c}^0$		$Y_c$
Cyclic tension 45°	$G_{12}^0, R_0, \beta, m$	$Y_{120}, Y_{12c}, Y_{12f}, \varepsilon_{12lim}$	$Z_{12}, G_{12}$
Compact Tension (CT)		$\varepsilon_{11tlim}, \varepsilon_{22tlim}$	$G_{It}, G_{IIt}$
Compact Compression (CC)		$\varepsilon_{11clim}, \varepsilon_{22clim}$	$G_{Ic}, G_{IIc}$

The specimens are made of commercial GG285P prepreg plies, produced by Toray. These plies consist of T700-12K plain weave carbon fabric, impregnated with DT120 high-toughness epoxy resin. All the samples are obtained from a single plate, which is cured in an autoclave at 120°C and 5 bar for 90 min and then cut to the final dimensions. The stacking sequence of the laminate is  $[0_f]_{12}$ . The specimens shape and size are chosen according to conventional ASTM standards for laminated composites, while CT and CC test method is derived from previous work of Pinho et al. [23].

In order to obtain the damage model parameters from experiments, the test results are elaborated using a procedure similar to that described in [16] and here adapted to the woven fabric material model. A detailed explanation of the calibration procedure is reported in Section 5.

Finally, quasi-static compressive crush tests are performed on corrugated CFRP specimens manufactured with the same fabric prepreg used for the coupon test campaign. The geometry of the samples, already employed in previous works [5,15,16], is adopted here in configurations using one, three, and five semi-circular patterns, hereafter denominated 1HC, 3HC, and 5HC. Two different stacking sequences are produced and tested, namely  $[0_f]_6$  and  $[45_f/45_f/0_f]_3$ , which result in specimens with a thickness of 2.10 and 2.15 mm, respectively. All samples have the same semi-circle radius of 6.5 mm and a height of 50 mm. The tests are conducted at a constant plate displacement rate of 5 mm/min until half of the total specimen height has been crushed.

#### 4. Experimental results

Experimental test results are described and listed below. Table 2 lists the test results for tensile and compressive tests of specimens loaded along the main orthotropy directions, here denoted as 11 and 22. At least three repetitions for every set have been conducted: the results report the average values of each set.

**Table 2.** Tensile and compressive tests results and calculated numerical input parameters.

Property	Description	Value
$E_{11t}$	Longitudinal tensile modulus	60.8 GPa
$E_{22t}$	Transverse tensile modulus	59.4 GPa
$E_{11c}$	Longitudinal compressive modulus	56.3 GPa
$E_{22c}$	Transverse compressive modulus	54.0 GPa
$\nu_{12}$	Poisson's ratio	0.04
$\sigma_{11t}$	Longitudinal tensile strength	1008 MPa

Three in-plane shear cyclic tensile tests are performed as shown in Figure 2. The in-plane shear damage model inputs for LV are calculated from the cyclic loadings as described in [21], and the damage parameters are reported in

**Table 3.**

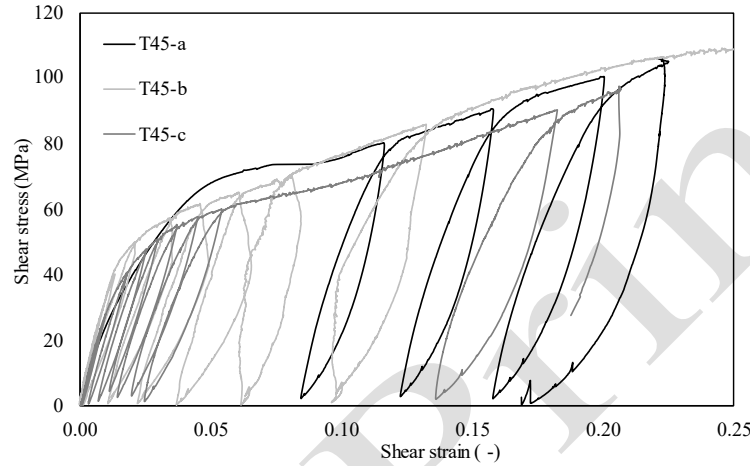


Figure 2. Example curves of cyclic tensile loading test on  $\pm 45$  laminates.

**Table 3.** In-plane shear results and calculated numerical input parameters.

Property	Description	Value
$G_{12}$	Shear modulus	3.3 GPa
$\sigma_{12,i}$	In-plane shear yield strength	17.8 MPa
$\sigma_{12,u}$	In-plane shear ultimate strength	65 MPa
$R_0$	Initial plasticity stress	10 MPa
$\beta$	Plasticity multiplier	0.304
$m$	Plasticity exponent	0.4368

#### 4.1 Compact Tension and Compact Compression tests

Three Compact Compression (CC) and four Compact Tension (CT) coupons are tested. In Figure 3, the load-displacement curves are shown. Fracture toughness values are calculated in accordance with the test procedure proposed by Pinho [23]; the main results are shown in Figure 4. Although the scatter in the experiments is significant, the compliance method has been found to give more consistent values for CC tests while the E399 method showed to be better suited for CT tests. In both cases, the data elaborations derive from fracture mechanics principles with the assumption that a single fracture plane develops during loading. In reality, due to the fiber weaving, multiple fracture paths are generated under tension, while fiber kinking and fragmentation occur under compression. Therefore, the reported fracture energies of CT and CC tests should be interpreted as volumetric averages of the multiple damage modes generated under tensile and compressive loads respectively.

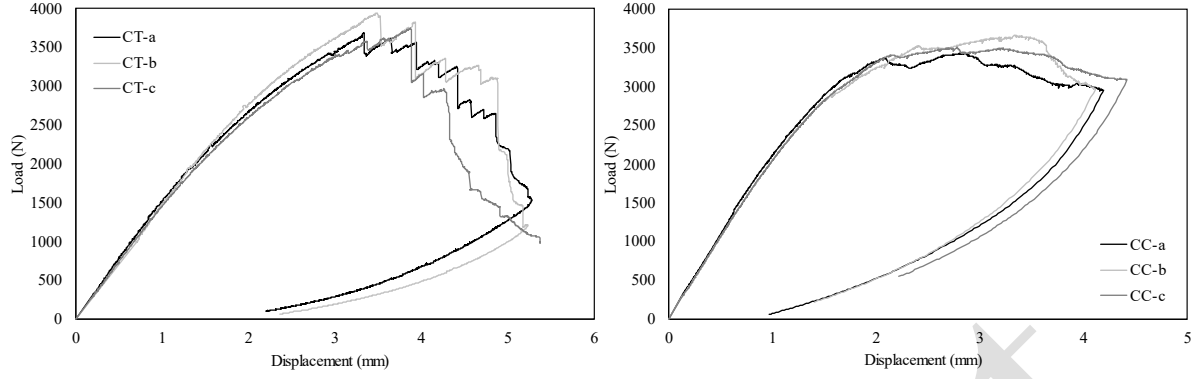


Figure 3. Load-Displacement curves for CT tests (left) and CC tests (right).

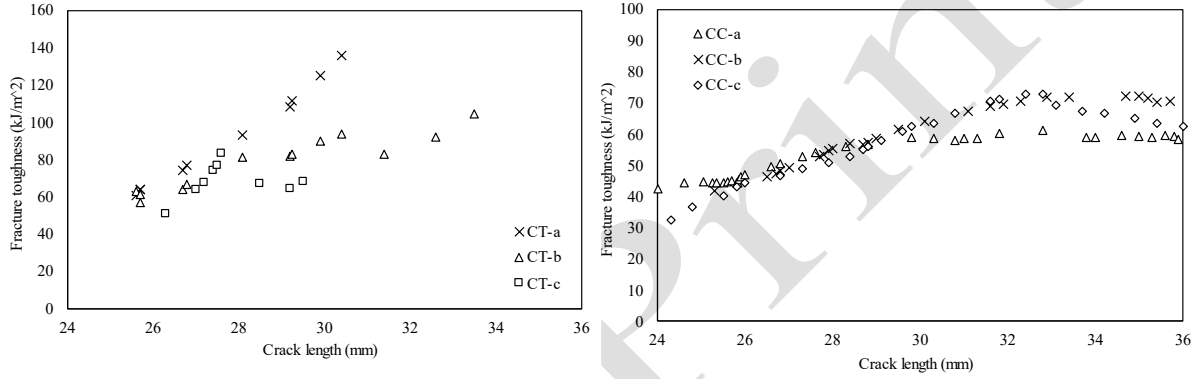


Figure 4.  $G_I$  values for tension (left) and compression (right) loading case. Compliance method values are shown for compressive tests, while E399 method values are reported for the tensile coupons.

#### 4.2 Crush tests

The test results for both stacking sequences and different coupon geometries are presented in Figure 5, while SEA values are summarized in Table 4. Here, the SEA is calculated as:

$$SEA = \frac{\int_0^L F dx}{\rho AL} \cong \frac{\bar{F}}{m_c} \quad (9)$$

Where  $\bar{F}$  is the average crush load throughout the total crosshead displacement  $L$ , and the crushed mass is calculated as  $m_c = mL/h$ , where  $h$  is the specimen height.

It is noticeable that, while the influence of the geometry on the load carrying capability is clear, its effect on the SEA seems less relevant. Comparing coupons with the same stacking sequence, in fact, SEA values vary within 5.4% and 3.8% respectively for  $[0_f]_6$  and  $[45_f/45_f/0_f]_5$ .

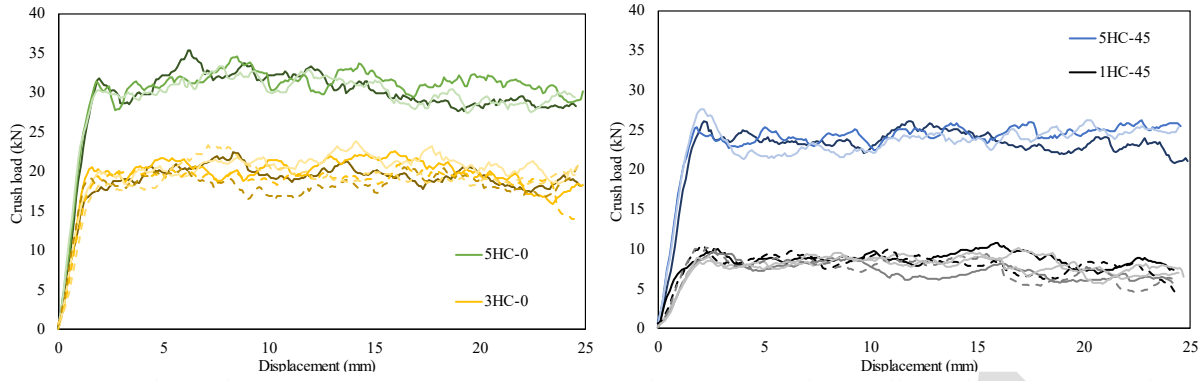


Figure 5. Load–Displacement results from compression crushing test. Results for all tested specimens are shown.

**Table 4.** Summary of crush tests specific energy absorption. Mean and standard deviation values are shown.

Layup	Group	# Repetitions	SEA (J/g)	
			$\mu$	$\sigma$
$[0_f]_6$	5HC_0	3	99.6	2.99
	3HC_0	6	104.5	3.47
$[45_f/45_f/0_f]_s$	5HC_45	3	86.3	2.88
	1HC_45	6	82.7	2.10

A limited scatter is observed across the three different geometries. In the following section, only the 5HC specimens are modeled and simulated, so to highlight the relevant differences between the two layups using a shared case.

## 5. Numerical Simulation

One peculiarity of crush simulation, that sets it apart from other scenarios where damage is predominant, is that loading is typically aligned with one axis of the component and contact pressure is uniformly distributed. Consequently, when damage is initiated in one element, the stress does not redistribute across neighboring elements (like for example under an impact type of loading). Instead, as damage leads to a reduction of the orthotropic stiffness along one specific direction, it will promote increasing deformation along that same path, which ultimately causes additional damage accumulation. For this reason, continuum models become quickly unstable as soon as the material properties impose a negative tangent stiffness.

Although the numerical models presented in Section 2 offer an exceptional flexibility, there is no guidance on how to obtain a valid calibration that maintains both adequate physical significance and stability in the solution phase. In this section, a streamlined procedure is introduced and exposed to efficiently calibrate the LV and WP damage models with minimal reliance on iterative methods and without the need for complex optimization algorithms.

To the best of the authors knowledge, established best practices to simulate the composite crushing are, to this date, rare and specialized to unique combinations of material and geometrical features. In fact, although several applications have been documented in the literature, little work has been done in proposing calibration methods that allows the designers to obtain a valid and reliable material card to be used in crush applications, spanning multiple scenarios.

### 5.1 LV model calibration strategy

In this paragraph, we clarify some of the details of the LV model as implemented in ESI-VPS. Moreover, some practical limitations of the model are exposed and resolved, allowing to simplify the determination of the damage parameters and giving rise to a straightforward procedure for optimal material calibration specific for crush simulation.

Firstly, in order to have numerical stability, we introduce a condition that guarantees positive tangent stiffness of the stress-strain relation. Rearranging Eq. (2-3), this condition is rewritten as in Eq. (10a) and Eq. (10b) for fiber and matrix modes respectively:

$$Y_{iif} = \frac{Y_{ii0} + Y_{iic}}{2} \quad (10a)$$

$$\ln(Y_{12f}) = \frac{\ln(Y_{120}) + Y_{12c}}{2} \quad (10b)$$

Furthermore, the modal damage parameters must be chosen in such a way that they do not introduce discontinuities in the stress-strain relation. In Figure 6, three damage evolution paths are shown for equal initiation and failure parameters  $Y_{ii0}$ ,  $Y_{iif}$  and different  $Y_{iic}$ . It shows that curve (2) is the only one that satisfies the smoothness of  $\sigma(\varepsilon)$ ; this condition is derived analytically in Eq. (11) under the shear mode, the linearity is recovered by taking the logarithms of  $Y$ .

$$Y_c = (Y_f - Y_0)/d_{max} \quad (11)$$

From Figure 6, it is also clear that the curve (3) is not acceptable because of the discontinuity at  $\varepsilon_f$  (Figure 6-b), while curve (1) has an undesirable behavior once the damage has reached the maximum value  $d = d_{max}$  and the material is still in the damage phase ( $\varepsilon < \varepsilon_f$ ).

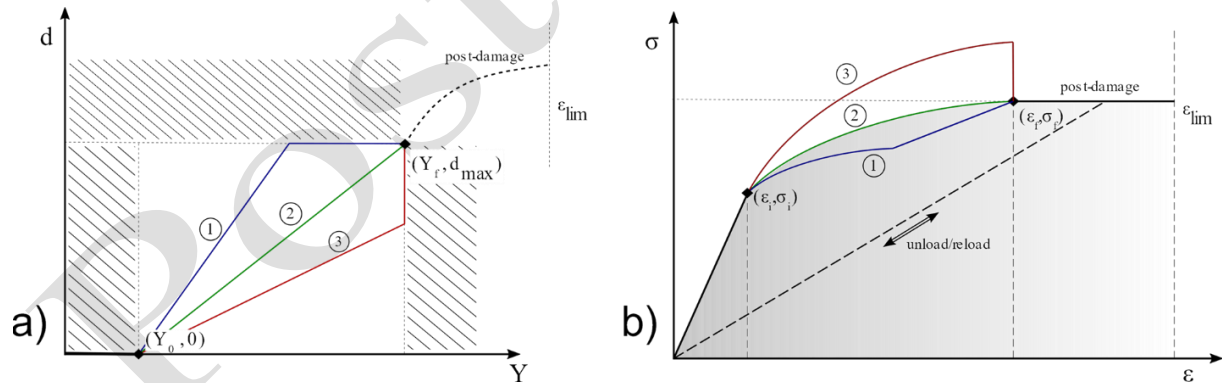


Figure 6. Behaviour of the Ladevèze damage with different input parameters. Effect of different  $d(Y)$  functions (a) on the stress-strain relation (b). Unload/reload path assumes no plasticity.

In the LV model, the initial and ultimate stress are not direct inputs of the material card but are derived from the damage functions. It is convenient, therefore, to have an explicit formulation by rewriting the damage functions as in Eq. (12). The latter can then be rewritten substituting Eq. (11) for  $d_{max}$  to obtain a quadratic function of  $Y_f$  with one positive root.

$$\sigma_i = \sqrt{2E_0 Y_0^2} \quad (12)$$

$$\sigma_f = \sqrt{2E_0 Y_f^2 (1 - d_{\max})^2} \quad (13)$$

The total strain energy to failure (shaded area in Figure 6-b) is finally controlled by the choice of an appropriate value of  $\varepsilon_{\lim}$  at which the element is eliminated and thus removed from the computation. This quantity is useful in controlling the output SEA during crash simulations and is calibrated from CT and CC tests.

The LV model, modified using the conditions previously discussed, allows to decouple the damage parameters without excessive loss of generality and performs properly in compressive crush simulations. This decoupling enables a straightforward procedure to calibrate the damage model. This, for fiber-oriented damage modes, looks as follows:

- 1) Calculate the undamaged Young's modulus  $E_0$  and find the stress  $\sigma_i$  at first nonlinearity from experimental tests.
- 2) Use Eq. (10a) to fix the initial damage parameter  $Y_0$ .
- 3) From experimental tests, obtain the ultimate failure stress  $\sigma_f$ .
- 4) Find the final damage limit  $Y_f$  by solving the quadratic expression  $Y_f^2 \sqrt{2E_0} = \sigma_f (2Y_f - Y_0)$  where each parameter is known.
- 5) Iteratively, determine the best fit value for the limit strains  $\varepsilon_{\lim}$  from direct simulations of CT and CC tests.

With this procedure, the model retains the main physical properties of the material, allowing at the same time a quicker calibration procedure acting only on a reduced number of free inputs. The modal element elimination strains are thus the only numerical inputs left to calibrate iteratively from CT, CC, and in-plane shear tests.

**Table 5.** LV damage parameters calibrated from experiments.

Property	Description	Value
$Y_{11t_0}$	Initial longitudinal tensile damage limit	0.09 GPa <sup>0.5</sup>
$Y_{11t_c}$	Yield longitudinal tensile damage limit	0.14 GPa <sup>0.5</sup>
$Y_{11t_f}$	Final longitudinal tensile damage limit	0.0914 GPa <sup>0.5</sup>
$D_{11 \max}$		0.01
$Y_{11c_0}$	Initial longitudinal compressive damage limit	0.0369 GPa <sup>0.5</sup>
$Y_{11c_c}$	Yield longitudinal compressive damage limit	0.0952 GPa <sup>0.5</sup>
$Y_{11c_f}$	Final longitudinal compressive damage limit	0.0589 GPa <sup>0.5</sup>
$D_{11c \max}$		0.021
$Y_{12_0}$	Initial shear damage limit	0.024 GPa <sup>0.5</sup>
$Y_{12_c}$	Yield shear damage limit	3.061 GPa <sup>0.5</sup>
$Y_{12_f}$	Final shear damage limit	0.0122 GPa <sup>0.5</sup>
$D_{12 \max}$	Post-damage level	0.42

## 5.2 WP model calibration strategy

The more recent WP model has a different approach to damaging compared to the traditional LV formulation and allows for an easier calibration procedure that explicitly fixes the maximum stress levels

and the fracture energies associated with each of the five damage modes. The failure envelope for damage initiation and the fracture energies for fiber-aligned fractures are directly obtained from experimental tests at failure and from CT and CC tests. Despite this simplicity, the model suffers from mesh sensitivity during crushing, as demonstrated later in Section 6.1. This phenomenon does not affect the calibration procedure but must be taken into account when different mesh sizes are used; the correction technique aims to recover the consistency of the strain energy density to failure and is addressed below.

The post-damage state for WP is set from numerical stability criteria and has no direct physical meaning. Furthermore, since element elimination follows the deviatoric strain, it cannot be decoupled for each fracture mode. This method trades simplicity for precision, as it is not possible to define uniquely the strain energy to failure for each failure mode, given that the post-damage state does not have fixed boundaries.

The post-damage state conditions are thus fixed to  $D_{max} = 0.85$  and  $\epsilon_{lim} = 0.15$  and these are not further modified in the model calibration.

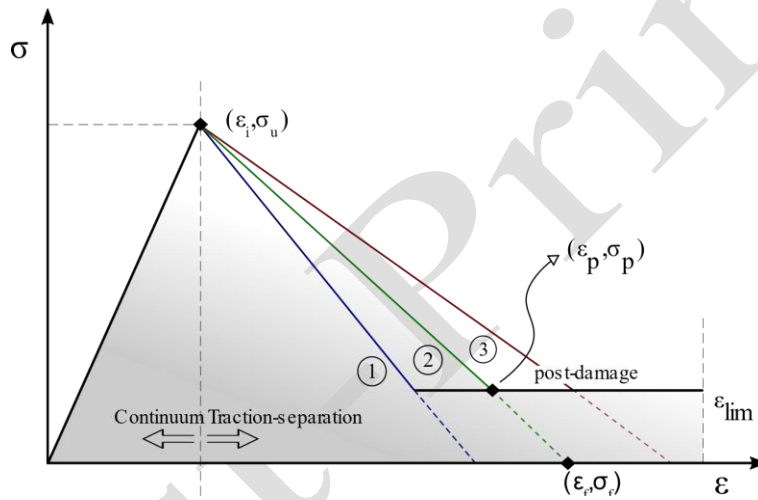


Figure 7. Behavior of the Waas-Pineda damage with different input parameters. Effect of different  $G_c$  functions on the stress-strain relation. The shaded area represents the total strain energy to failure for the curve (2).

Hence, a logical procedure to calibrate the WP model looks as follows:

- 1) From experimental tests, obtain the ultimate failure stresses  $\sigma_{ij}^f$ .
- 2) Set the ultimate stresses as stress thresholds for damage initiation.
- 3) Calculate the fiber fracture energies from CT and CC tests and apply them to the model.
- 4) Fix  $D_{max}$  and  $\epsilon_{lim}$  to fulfil the numerical stability criterion.

Concerning the in-plane shear damage mode, the modal fracture energy is obtained by equating the total strain energy to failure with experimental tests, using trapezoidal integration of the stress-strain curve of the tensile tests. For the fiber-aligned fracture energies, the influence of experimental scatter on the numerical models is evaluated by simulating the test with increased and reduced parameters; the results are reported in the following section.

**Table 6.** WP damage parameters calibrated from experiments.

Property	Description	Value
$X_t$	Longitudinal tensile initiation stress	1008 MPa
$X_c$	Longitudinal compressive initiation stress	598 MPa

$Y_t$	Transverse tensile initiation stress	958 MPa
$Y_c$	Transverse compressive initiation stress	578 MPa
$Z_{12}$	In-plane shear initiation stress	65 MPa
$G_{It}$	Longitudinal tensile fracture energy	0.105 kJ/m <sup>2</sup>
$G_{Ic}$	Longitudinal compressive fracture energy	0.085 kJ/m <sup>2</sup>
$G_{II t}$	Transverse tensile fracture energy	0.105 kJ/m <sup>2</sup>
$G_{II c}$	Transverse compressive fracture energy	0.085 kJ/m <sup>2</sup>
$G_{12}$	In-plane shear fracture energy	0.038 kJ/m <sup>2</sup>

### 5.3 Fracture energy corrections for WP model

The fracture energies used as input in the WP model are equivalent to energy release rates corresponding to the theoretical fracture generated inside the finite element. The characteristic of the WP model is that only one fracture plane per damage mode is allowed to exist within one element; therefore, a finer discretization, effectively allowing a higher number of fracture surfaces, ultimately leads to a higher total fracture energy available to be dissipated. This effect becomes critical in crush scenarios, where the failure mode is dominated by fragmentation and the fracture density is lost at the typical discretization scales allowed by FEM. For this reason, to avoid incurring in mesh sensitivity, the fracture energy must be defined in a broader sense to recover the consistency of the strain energy density.

This phenomenon is shown graphically in Figure 8 for two different meshes: when only one fracture is allowed in the model (a.), the total dissipated energy is proportional to the surface area given by the internal length  $l_f$  and the element thickness  $w$ . If the input fracture energy is unchanged, reducing the mesh size in half (b.) consists in doubling the total surface area accounting for damage, thus the total energy that can be dissipated is increased twofold. In (c.) the mesh objectivity is restored with a correction of the fracture energy, which guarantees the equivalency of the total dissipated energy in the unit volume.

Concisely, the consistency of the energy density  $e_D$  is recovered by Eq. (14), where the fracture energies calculated in Section 4.1 are understood as the energy release rates dissipated in a unitary volume.

$$e_D = \frac{G_{cii}}{l_{fi}} = const \quad (14)$$

This approach, although following a different path, is essentially equivalent to the solution adopted by Reiner et. al. [24]. In their work, the Bažant crack band scaling is first implemented in two numerical models to maintain objectivity in conventional fracture application, and ultimately it is found that the scaling is not applicable in progressive crush simulations, where the dissipated energy must be maintained at different element sizes.



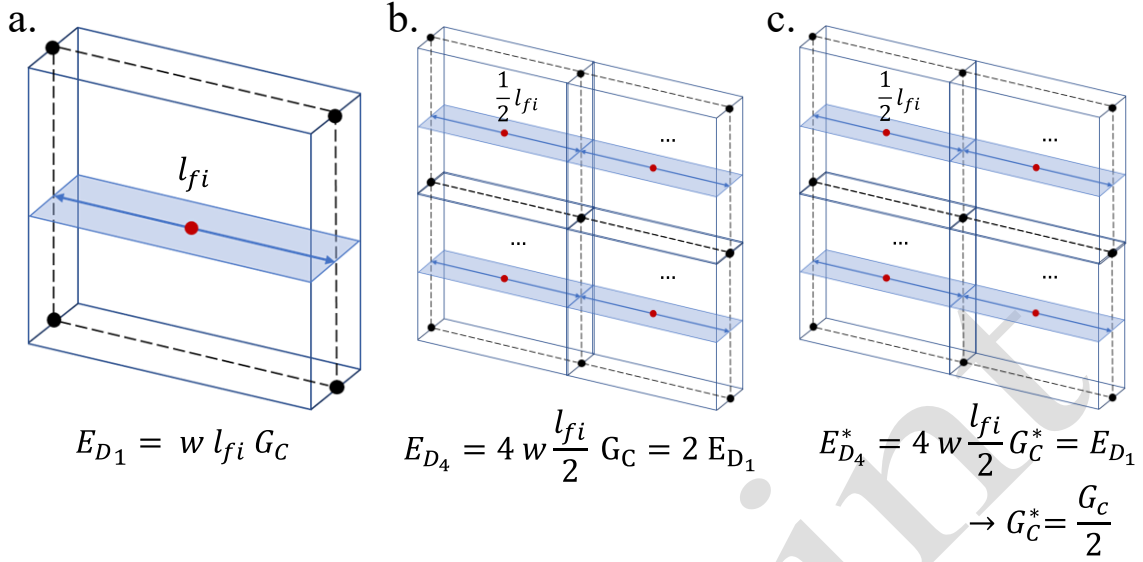


Figure 8. Without correction of the fracture energy  $G_C$ , the total strain energy is inconsistent at different mesh densities (a., b.). When the fracture energy is corrected at the finer mesh (c.) the strain energy density is recovered.

#### 5.4 Calibration on CT and CC tests

The numerical models for CT and CC are built using a single shell with multi-layered formulation. The notch region was discretized with elements of 0.2 mm length and the out-of-plane displacement was constrained in order to remove undesired buckling. The load was applied by prescribing a constant displacement at the two loading regions via a multi-point constraint, leaving rotation around the out-of-plane axis free. In the CT model, the notch is realized by a V-shape mesh offset (Figure 9). Different notch configurations have been evaluated, showing a minimal influence on the overall load response.

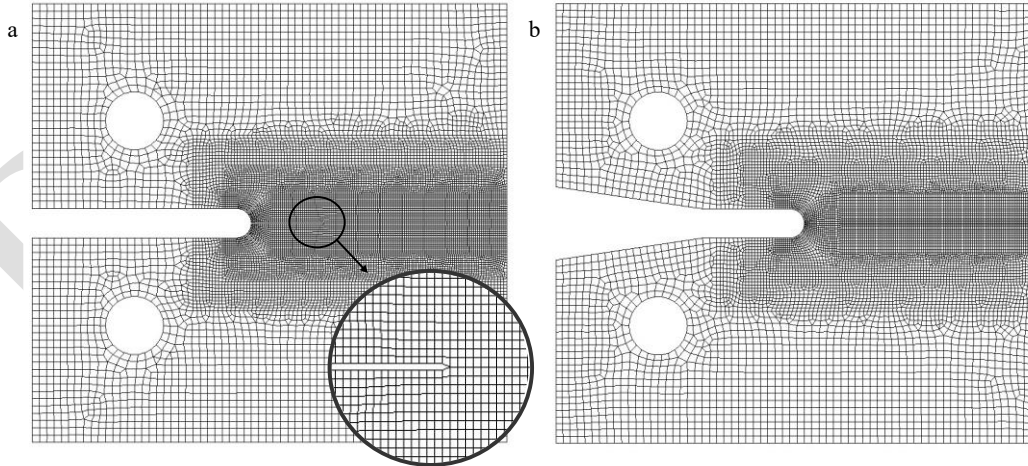


Figure 9. Example mesh used for CT (left) and CC (right) simulations. The element size around the notch is 0.2 mm, and far from the stress concentration is 1 mm. A magnification of the V-shaped notch region at the crack tip of the CT model is shown.

The tuning of the free inputs for the LV model is shown in Figure 10, where the calibrated model is highlighted in red and the respective elimination strains are reported in Table 7. Due to the scatter measured in CT and CC tests, a sensitivity study on the WP model is carried out to evaluate the effect of fracture

energies inputs on the resulting load (Figure 11). It should be noted that here the mesh density does not affect the results in the WP model, since damage only affects a single row of elements.

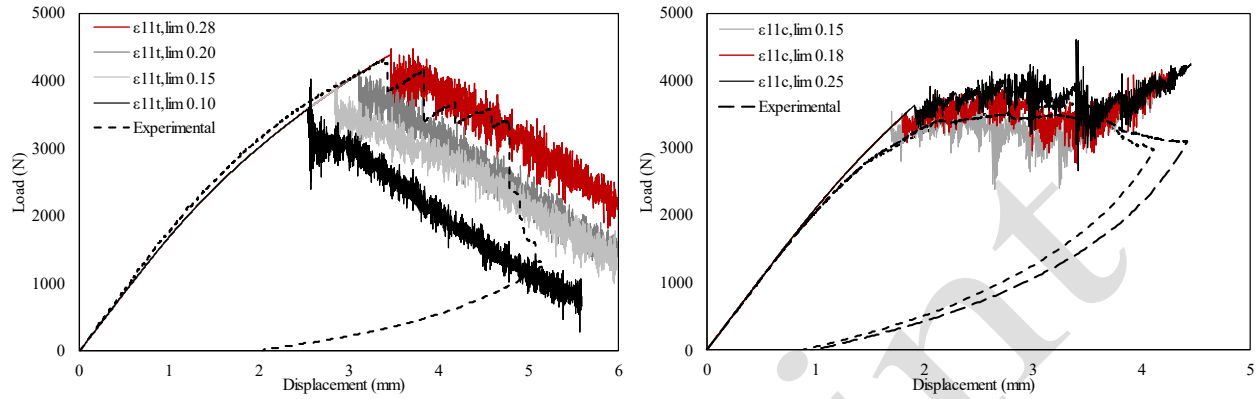


Figure 10. Comparison of experimental and simulated load-displacement output for CT (left) and CC (right) models using the LV model at different element elimination strain thresholds. Calibrated model highlighted in red.

In the CC models, the contact algorithm is introduced to compensate for the loss of material deriving from the elimination of elements as the crack tip advances. This is necessary to maintain a stable propagation, but it causes the models to break at elevated deformations. The effect is seen in Figure 10, where all simulations converge to similar results after 3 mm displacement, as a result of the contact algorithm overcoming the damage criterion. The same applies to the WP model below (Figure 11).

**Table 7.** Calibrated values of the elimination algorithm inputs for LV damage.

Property	Description	Value
$\varepsilon_{11t}$	Longitudinal tensile limit strain	0.28
$\varepsilon_{11c}$	Longitudinal compressive limit strain	0.15
$\varepsilon_{22t}$	Transverse tensile limit strain	0.28
$\varepsilon_{22c}$	Transverse compressive limit strain	0.15
$\varepsilon_{12}$	In-plane shear limit strain	0.6

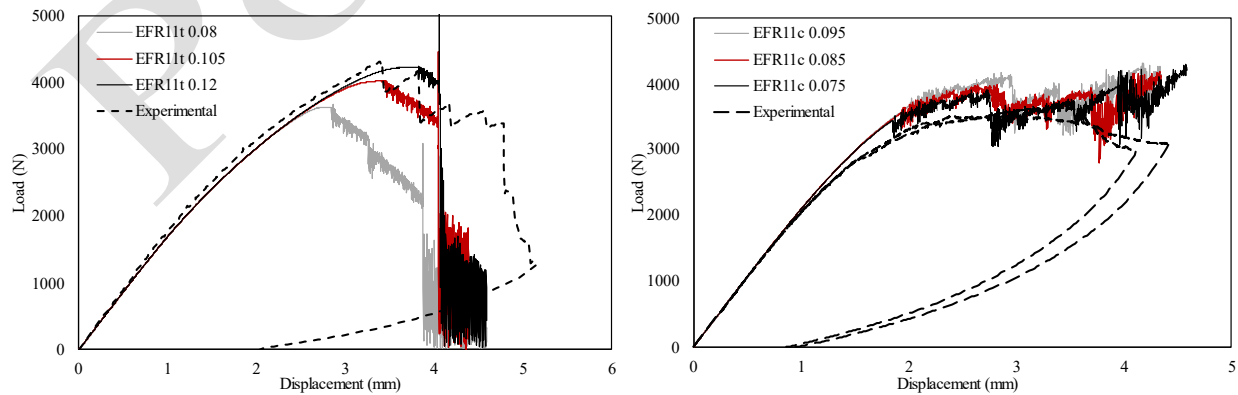
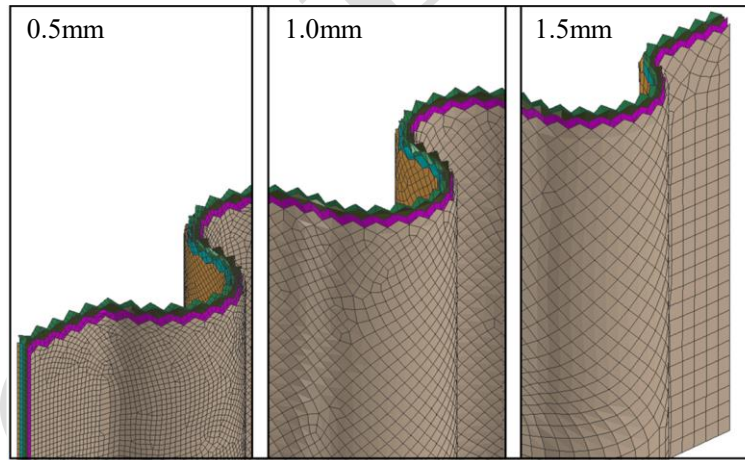


Figure 11. Comparison of experimental and simulated load-displacement output for CT (left) and CC (right) models using the WP model at different fracture energy values. Model derived from experimental values highlighted in red.

## 6. Crush test validation

The crush models are built from shell elements using six stacked plies. The load is shared across adjacent plies through tied links with included damage from a traditional interlaminar cohesive formulation. The bilinear cohesive model is taken from previous work on a similar unidirectional composite material [16] sharing the same matrix system as the fabric material investigated here. The influence of the cohesive model on the overall crush response is evaluated below. The trigger region consists of a combination of sawtooth shape and node offset from the midplane, to encourage ply splaying and reduce the risk of instability after the initial peak load. The effect of mesh configuration on the numerical crush load stability has been investigated thoroughly in [24], showing that better results are found when using skewed or unstructured mesh, as opposed to oriented mesh. The unstructured mesh configuration at 1 mm target element side length, shown in Figure 12, consists in 30k elements and is used as baseline configuration. Additional tests at smaller (0.5 mm, 120k elements) and larger (1.5 mm, 15k elements) mesh sizes are reported in Section 5.5. The use of cohesive elements for the lamina interfaces prohibits the choice of larger elements, since their conditional stability is well documented in the literature and in a previous work by the authors [16]. The bottom nodes of the model are constrained in all degrees of freedom, while the top crushing plate is modeled as a rigid body with an imposed velocity of 1 mm/ms. The explicit time integration step is  $2.3\text{E-}5$  ms and no dynamic mass scaling is used to speed up the computation. The simulation is stopped after 25 ms internal time, equivalent to 25 mm of crushed length. The elapsed runtime using 24 parallel processing units is 1 hour for the coarse mesh, 2.5 hours for the baseline mesh and 8.5 hours for the fine mesh.



*Figure 12. Detail of the unstructured mesh and the trigger region at the three discretization levels. The top nodes of the two central plies are offset by 0.2 mm from the midplane to improve splaying. Tied links between adjacent plies are not shown.*

The load-displacement and SEA results of the four baseline simulation cases (5HC-0 and 5HC-45 layups, with both LV and WP damage models) are shown below. These distinct cases additionally share inputs related to the interlaminar model, contact algorithms, and stability criteria. The baseline cohesive interlaminar fracture energies are  $470 \text{ J/m}^2$  and  $1790 \text{ J/m}^2$  for Mode I and Mode II respectively. The cohesive stiffness and traction limits have been calibrated in a previous campaign and can be found in [16].

The contact interaction between the damaged plies and the rigid wall is modeled with 0.2 Coulomb friction coefficient. When the inter-ply tied links are removed after ultimate interface damage, the adjacent plies are allowed to transfer load through a contact interaction with 0.4 friction coefficient. The calibrated baseline results are shown in Figure 13 below. In accordance with the experimental campaign, the

numerical SEA is calculated taking into consideration the full loading curve up to 25 mm crushed length, while the crushed mass is derived from the model mass.

The results related to the baseline 1.0 mm mesh size indicate that the calibration of both models leads to a satisfactory prediction of the crushing energy, with an error of 0.8% and 5.6% for the LV model in the  $[0]_6$  and  $[45_2/0]_s$  layups respectively. Comparatively, the WP models have a 12% and 5.6% error with respect to experimental values. In addition, the load curves show limited oscillations, bounded within  $\pm 3.5$  kN under all configurations. Different trigger configurations were investigated in a previous work [16], indicating that the trigger only affects the initial region of the load curve, while the steady-state region is unaffected. In this work, despite the use of a sophisticated geometric trigger mechanism, the initial peak load is not eliminated.

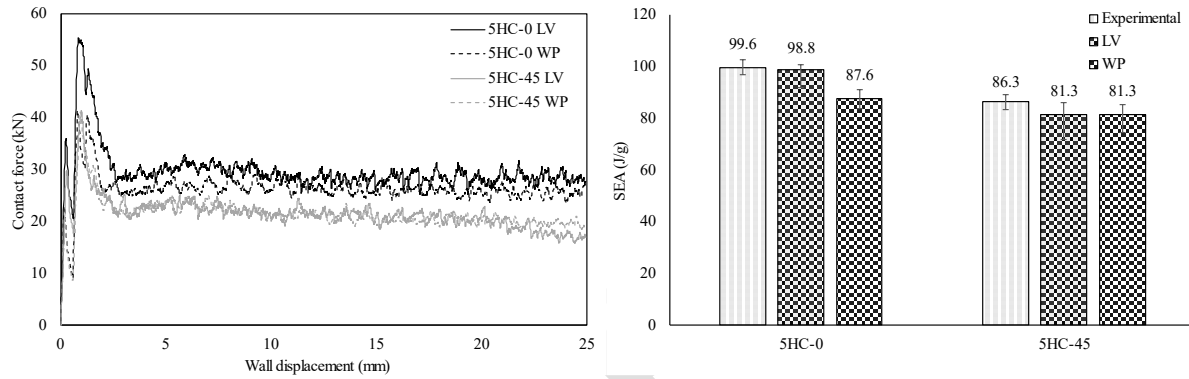


Figure 13. Calibrated force-displacement curves (left) and resulting SEA compared to test data (right). Error bars represent the standard variation scatter in the quasi-static region (5-25mm).

### 6.1 Mesh objectivity

The LV damage formulation is calibrated from the global strain energy density to failure; therefore, it does not suffer from mesh sensitivity, as can be seen from the numerical results at the three different mesh sizes in Figure 14. Nevertheless, the smaller mesh discretization yields to a moderately higher sustained load and consequently higher SEA. The morphology of damage after 10 mm of plate displacement (Figure) clearly shows that the 0.5 mm mesh is characterized by more tearing and element erosion compared to the runs with 1.0 mm and the 1.5 mm meshes, ultimately leading to a higher dissipation of energy. Nevertheless, the results are only slightly affected, with a maximum of 10% SEA increase on  $[0]_6$  and 6% on  $[45_2/0]_s$  laminates.

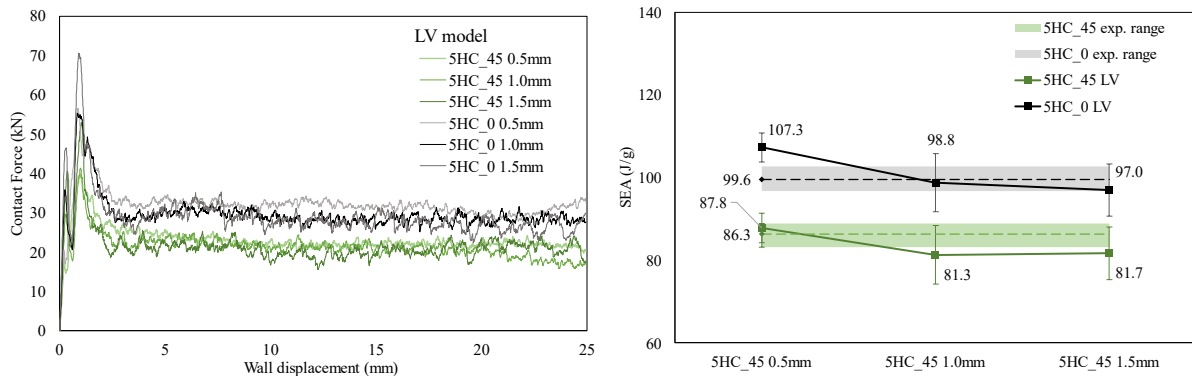


Figure 14. Mesh sensitivity study with the LV damage model for the two investigated laminates. Numerical outputs of the force-displacement plots (left), numerical and experimental SEA (right).

The results for the WP model are highlighted in Figure 15: as anticipated in Section 5.3, the default material card calibrated according to the proposed procedure can only produce accurate results for a given mesh configuration, namely the 1 mm mesh; varying the element size leads to poor performance.

When the material card is corrected with respect to the consistency of the strain energy, the mesh objectivity is greatly recovered, although the results, similarly to the LV case, still retain some scaling effects. Again, Figure shows that the finer elements generate a different failure profile: more fragmentation and element erosion is observed after 10 mm of crush plate displacement, whereas the larger mesh is more prone to generate slaying and folding of the plies.

With both numerical models, the finer mesh appears to bring an overall improvement in the fidelity of the results, although a definite overestimation of the SEA is observed in two cases: 5HC-45 WP and 5HC-0 LV.

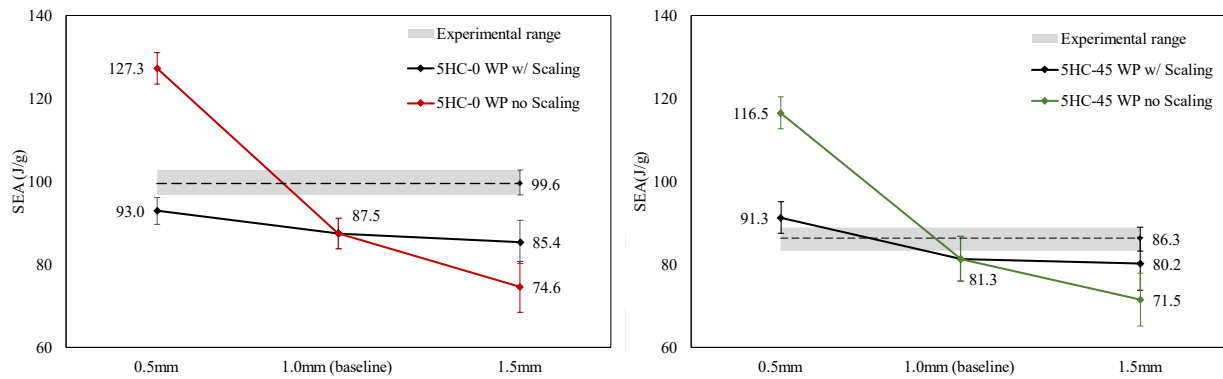


Figure 15. Simulated SEA for WP models at different mesh sizes. Comparison between default (coloured line) and corrected (black line) material model inputs; shaded area represents the test results range.



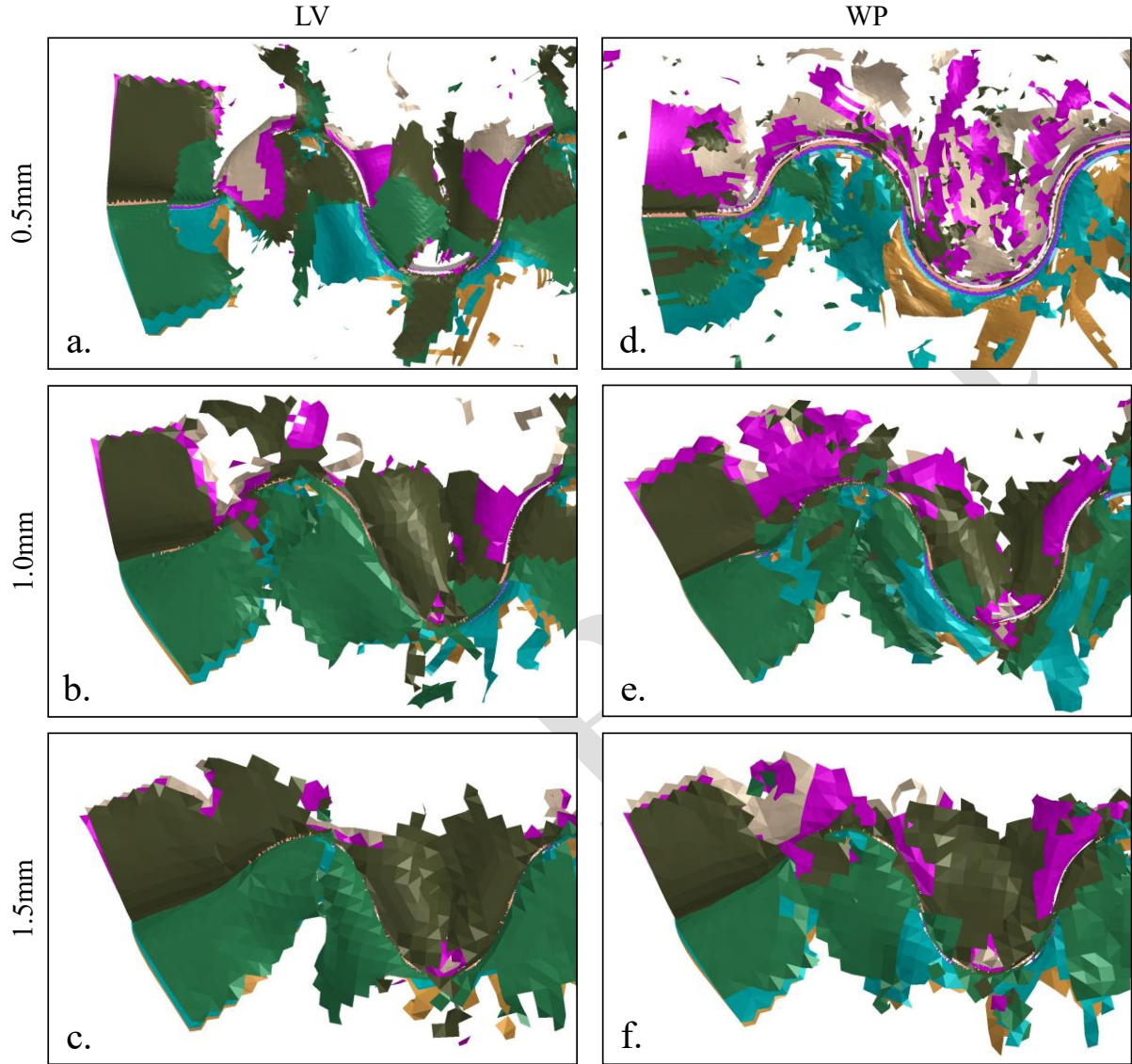


Figure 16. Morphology of damage at 10 mm of crushed displacement for different mesh sizes (0.5 mm: a., d., 1.0 mm b., e., 1.5 mm c., f.) and numerical models (Ladevèze: a., b., c., Waas-Pineda: d., e., f.). The WP contours are relative to the inputs with corrected fracture energies.

## 6.2 Sensitivity analysis on secondary parameters

A study is carried out on the effects of interlaminar toughness and friction algorithms on the dissipated energy, with particular focus on the on the load curve profile, peak load and SEA.

Firstly, interlaminar Mode I and Mode II fracture toughness values are investigated: the interlaminar damage is scaled with respect to the baseline calibration by increasing the fracture energy and the initial traction consistently. This is chosen in order to maintain the cohesive zone length constant, to avoid alterations of the morphology of the damage. The fracture energies (EFRAC) are thus evaluated at 2x, 4x, and 0.5x with respect to the baseline. The comparison here is limited to the single case of the 5HC-45 LV. The results, shown in Figure 16, indicate that the baseline value is the one that performs better in the tested configuration. The other values yield either a less stable load or a significantly lower sustained load for the 4x case. This effect is made clear by comparing the contour plots of the cohesive damage at 10 mm crushed

displacement, representative of the steady-state zone (Figure 17): the baseline model is the condition with the shortest damaged zone. This allows to have a more stable crushing profile and, therefore, a load curve that remains at a more constant load throughout the displacement range. From the 4x case it is evident, surprisingly, that a too stiff cohesive response does not guarantee either a higher sustained load or a stable crush profile.

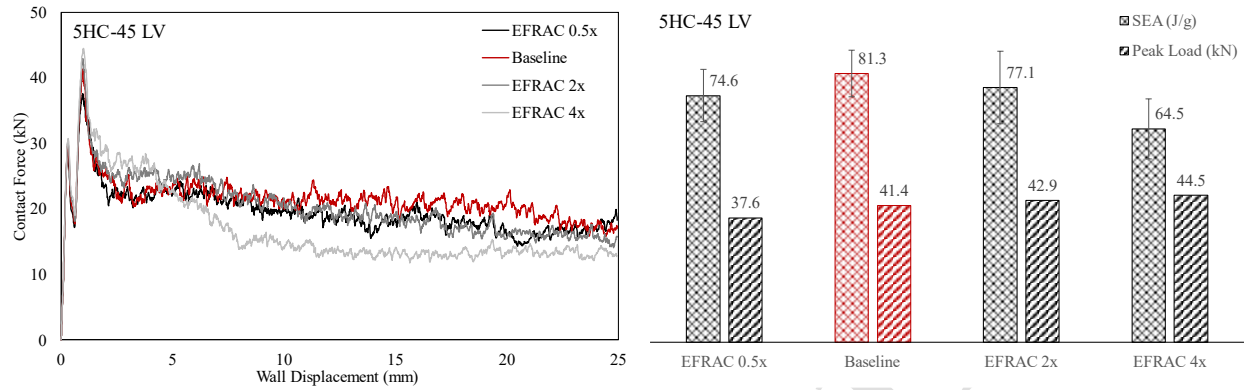


Figure 16. Comparison of numerical simulation of the 5HC-45 LV model at different interlaminar fracture toughness: crush force load curves (left), SEA, and peak load (right). Calibrated model (baseline) highlighted in red.

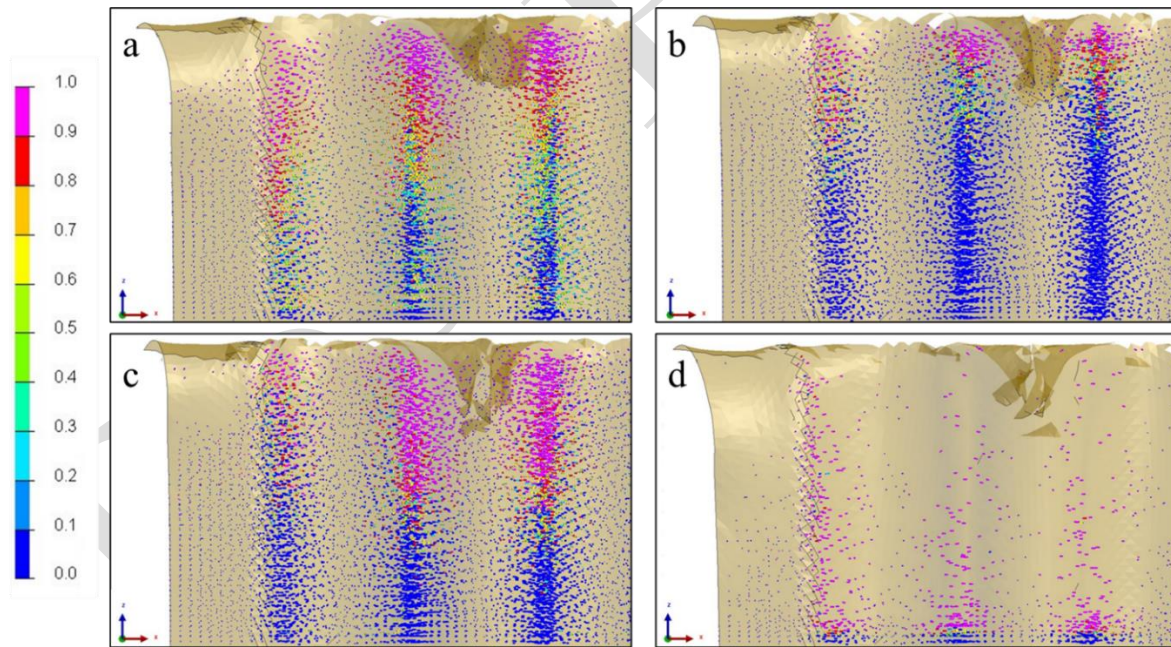


Figure 17. Comparison of cohesive damage contour plots after 10 mm crushed height: a) 0.5x fracture toughness, b) baseline, c) 2x fracture toughness d) 4x fracture toughness.

The process of CFRP compressive crushing generates high frictional forces at the wall in contact with the damaging specimen and across delaminated plies. While some researchers carried out studies evaluating the extent of frictional forces in damaging components [25], an accurate estimation of the forces during crushing is difficult to obtain. Instead, most numerical models rely on standardized values used for impact simulations and other scenarios.

In this section, different values of Coulomb friction coefficients are compared in the base 5HC-45\_LV model. For the contact between the specimen and the rigid wall, the values investigated were 0, 0.2, 0.4, 0.6, and 0.8, while for self-contact of plies, the coefficient was varied between 0, 0.4, and 0.8. For ease of comparison, a full factorial campaign was not performed. Instead, the baseline values were set to 0.2 and 0.4 for the wall contact and self-contact respectively, and only one of the two contact pairs was modified each time. The results are reported in Figure 18, showing the SEA and peak force of each configuration.

Whereas increasing friction coefficients is initially correlated with increased SEA, an excessive friction can effectively reduce the sustained crush load, leading to unstable failure. Indeed, Figure 19 and Figure 20 show the morphology of the crushed specimens in the simulated and experimental case at varying values of the wall contact friction. It is evidenced that a higher friction between the rigid wall and the specimen contrasts the splaying of the outer plies and leads the coupon to fold onto itself (a configuration that is not supported by experimental evidence).

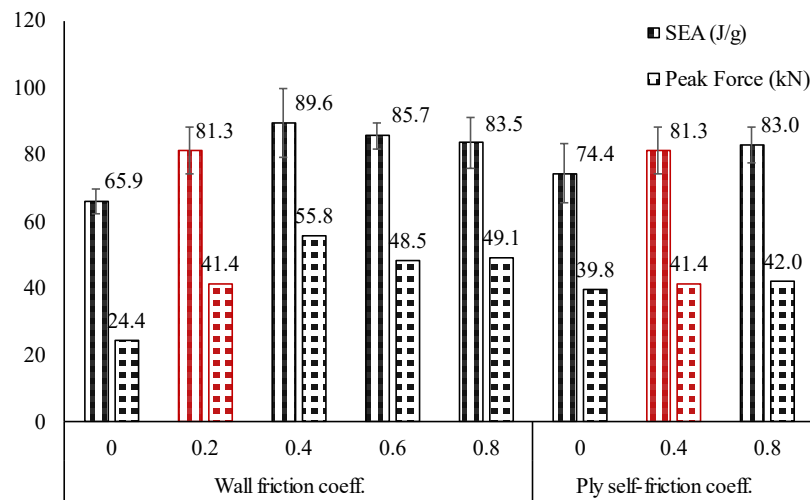


Figure 18. Comparison of numerical simulation of the 5HC-45 LV model at different contact friction coefficients: SEA and peak load values. Calibrated model (baseline) highlighted in red. Error bars represent the standard variation in the quasi-static region (5-25 mm)

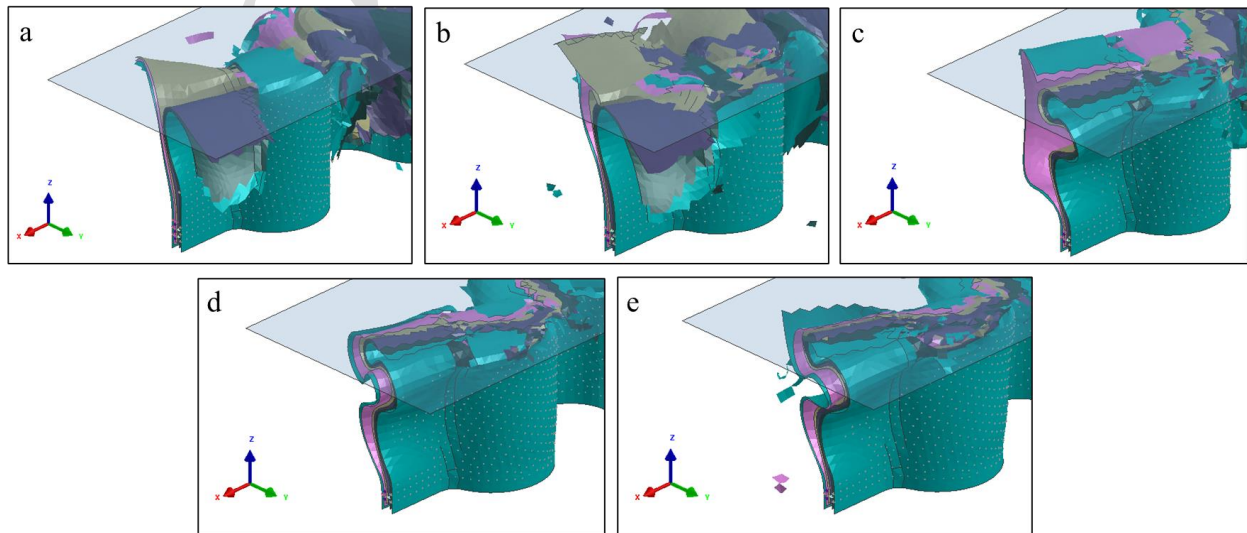




Figure 19. Comparison of ply deformation at the free edge after 20mm crushed height at different wall contact friction coefficients a) no friction b) 0.2 baseline, c) 0.4 d) 0.6 e) 0.8.



Figure 20. Example of lateral ply splaying for  $[0]_6$  layup (left) and  $[45/0]_s$  layup (right).

## 7. Conclusions

The energy absorbed during crushing of woven fiber CFRP is simulated via FEM analysis using the explicit solver of ESI-VPS. Two damage models are implemented and compared: Ladevèze model, which uses ply-level continuum damage mechanics, and Waas-Pineda model, which uses discrete traction-separation laws to model smeared cracks within the continuum elastic-plastic formulation.

The two numerical models for damage are suitable for a wide range of applications, but crash simulations impose additional constraints in the shape of the damage curves, to remove the occurrence of numerical instabilities. A calibration procedure has been implemented for LV and WP models to avoid instabilities while minimizing the need for iterative procedures. Compact Tension and Compact Compression tests are found to be useful in recreating, in a controlled environment, the failure and fracture propagation phenomena that occur during crushing. Therefore, they are used as reference load cases for calibration of the material cards: it is shown that replicating the CT and CC load cases in the numerical environment is effective in obtaining satisfactory results using both Ladevèze and Waas-Pineda models for the compressive crush scenario.

Coupons with corrugated geometry and two different layups are tested, and the results are replicated in the FE environment using an orthotropic stacked shell with unstructured mesh. Interlaminar damage is included using a cohesive formulation. Both calibrated models show satisfactory results under all scenarios, being able to capture the absorbed energy with a maximum error well below 15%.

The mesh sensitivity of the two numerical models is also investigated: with LV, the variation of SEA for three different element sizes is well controlled since the model is calibrated at constant strain energy at failure. Instead, the WP model is based on fracture energy quantities that do not scale correctly with mesh size in progressive crushing applications. When the correction scheme is applied, to recover the consistency of energy density, the variation in SEA is significantly reduced.

Finally, the interlaminar fracture toughness and contact frictions are investigated: it is shown that an adequate calibration is necessary, as both interlaminar model and contact friction algorithms show a nonlinear correlation to inputs parameters. In particular, adequate interlaminar damage is greatly responsible for crush stability, as values that are either too high or too low may equally lead to irregular delamination patterns with extensive delaminated areas. The authors believe that further investigations are

required on this specific topic, as, currently, no guidelines are available to adjust the interlaminar damage models in order to assure stable crushing load under different conditions.

### Data Availability

The raw/processed data required to reproduce these findings cannot be shared at this time due to technical or time limitations.

### References

- [1] Ramakrishna S, Hamada H, Maekawa Z, Sato H. Energy Absorption Behavior of Carbon-Fiber-Reinforced Thermoplastic Composite Tubes. *J Thermoplast Compos Mater* 1995;8:323–44. <https://doi.org/10.1177/089270579500800307>.
- [2] Chang IY, Lees JK. Recent Development in Thermoplastic Composites: A Review of Matrix Systems and Processing Methods. *J Thermoplast Compos Mater* 1988;1:277–96. <https://doi.org/10.1177/089270578800100305>.
- [3] Cauchi Savona S, Hogg PJ. Effect of fracture toughness properties on the crushing of flat composite plates. *Compos Sci Technol* 2006;66:2317–28. <https://doi.org/10.1016/j.compscitech.2005.11.038>.
- [4] Thornton PH, Harwood JJ, Beardmore P. Fiber-reinforced plastic composites for energy absorption purposes. *Compos Sci Technol* 1985;24:275–98. [https://doi.org/10.1016/0266-3538\(85\)90026-0](https://doi.org/10.1016/0266-3538(85)90026-0).
- [5] Feraboli P. Development of a corrugated test specimen for composite materials energy absorption. *J Compos Mater* 2008;42:229–56. <https://doi.org/10.1177/0021998307086202>.
- [6] Jacob GC, Fellers JF, Simunovic S, Starbuck JM. Energy absorption in polymer composites for automotive crashworthiness. *J Compos Mater* 2002;36:813–50. <https://doi.org/10.1177/0021998302036007164>.
- [7] Ramakrishna S, Hamada H. Energy absorption characteristics of crash worthy structural composite materials. *Key Eng Mater* 1998;141–143:585–620. <https://doi.org/10.4028/www.scientific.net/kem.141-143.585>.
- [8] Troiani E, Donati L, Molinari G, Di Sante R. Influence of Plying Strategies and Trigger Type on Crashworthiness Properties of Carbon Fiber Laminates Cured through Autoclave Processing. *Strojniški Vestn – J Mech Eng* 2014;60:375–81. <https://doi.org/10.5545/sv-jme.2013.1506>.
- [9] Jiang H, Ren Y, Gao B. Research on the progressive damage model and trigger geometry of composite waved beam to improve crashworthiness. *Thin-Walled Struct* 2017;119:531–43. <https://doi.org/10.1016/j.tws.2017.07.004>.
- [10] Kohlgruber D. Improved Simulation Methodologies to Model the Crash Behaviour of Composite Structures. Stuttgart: n.d.
- [11] Hanagud S, Craig JJ, Sriram P, Zhou W. Energy Absorption Behavior of Graphite Epoxy Composite Sine Webs. *J Compos Mater* 1989;23:448–59. <https://doi.org/10.1177/002199838902300502>.
- [12] Cauchi Savona S, Hogg PJ. Investigation of plate geometry on the crushing of flat composite

- plates. *Compos Sci Technol* 2006;66:1639–50. <https://doi.org/10.1016/j.compscitech.2005.11.011>.
- [13] Price JN, Hull D. Axial crushing of glass fibre-polyester composite cones. *Compos Sci Technol* 1987;28:211–30. [https://doi.org/10.1016/0266-3538\(87\)90003-0](https://doi.org/10.1016/0266-3538(87)90003-0).
  - [14] Chang FK, Chang KY. A Progressive Damage Model for Laminated Composites Containing Stress Concentrations. *J Compos Mater* 1987;21:834–55. <https://doi.org/10.1177/002199838702100904>.
  - [15] Feraboli P, Wade B, Deleo F, Rassaian M, Higgins M, Byar A. LS-DYNA MAT54 modeling of the axial crushing of a composite tape sinusoidal specimen. *Compos Part A Appl Sci Manuf* 2011;42:1809–25. <https://doi.org/10.1016/j.compositesa.2011.08.004>.
  - [16] Rondina F, Donati L. Comparison and validation of computational methods for the prediction of the compressive crush energy absorption of CFRP structures. *Compos Struct* 2020;254:112848. <https://doi.org/10.1016/j.compstruct.2020.112848>.
  - [17] Ladevèze P. A damage computational method for composite structures. *Comput Struct* 1992;44:79–87. [https://doi.org/10.1016/0045-7949\(92\)90226-P](https://doi.org/10.1016/0045-7949(92)90226-P).
  - [18] Ladevèze P, Allix O, Gornet L, Lévêque D, Perret L. A computational damage mechanics approach for laminates: Identification and comparison with experimental results. *Stud Appl Mech* 1998;46:481–500. [https://doi.org/10.1016/S0922-5382\(98\)80059-7](https://doi.org/10.1016/S0922-5382(98)80059-7).
  - [19] Ladeveze P, LeDantec E. Damage modelling of the elementary ply for laminated composites. *Compos Sci Technol* 1992;43:257–67. [https://doi.org/10.1016/0266-3538\(92\)90097-M](https://doi.org/10.1016/0266-3538(92)90097-M).
  - [20] Pineda EJ, Waas AM. Numerical implementation of a multiple-ISV thermodynamically-based work potential theory for modeling progressive damage and failure in fiber-reinforced laminates. *Int J Fract* 2013;182:93–122. <https://doi.org/10.1007/s10704-013-9860-1>.
  - [21] Johnson AF, Pickett AK, Rozycki P. Computational methods for predicting impact damage in composite structures. *Compos Sci Technol* 2001;61:2183–92. [https://doi.org/10.1016/S0266-3538\(01\)00111-7](https://doi.org/10.1016/S0266-3538(01)00111-7).
  - [22] Pineda EJ. A Novel Multiscale Physics-Based Progressive Damage and Failure Modeling Tool for Advanced Composite Structures. University of Michigan, 2012.
  - [23] Pinho ST, Robinson P, Iannucci L. Fracture toughness of the tensile and compressive fibre failure modes in laminated composites. *Compos Sci Technol* 2006;66:2069–79. <https://doi.org/10.1016/J.COMPSCITECH.2005.12.023>.
  - [24] Reiner J, Feser T, Waimer M, Poursartip A, Voggenreiter H, Vaziri R. Axial crush simulation of composites using continuum damage mechanics: FE software and material model independent considerations. *Compos Part B Eng* 2021;225:109284. <https://doi.org/10.1016/j.compositesb.2021.109284>.
  - [25] Pinho ST, Camanho PP, De Moura MF. Numerical simulation of the crushing process of composite materials. *Int J Crashworthiness* 2004;9:263–76. <https://doi.org/10.1533/ijcr.2004.0287>.